

Flow reversals in Rayleigh–Bénard convection with non-Oberbeck–Boussinesq effects

Shu-Ning Xia¹, Zhen-Hua Wan^{1,†}, Shuang Liu¹, Qi Wang¹
and De-Jun Sun^{1,†}

¹Department of Modern Mechanics, University of Science and Technology of China,
Hefei 230027, China

(Received 3 February 2016; revised 26 April 2016; accepted 12 May 2016)

Flow reversals in two-dimensional Rayleigh–Bénard convection led by non-Oberbeck–Boussinesq (NOB) effects due to large temperature differences are studied by direct numerical simulation. Perfect gas is chosen as the working fluid and the Prandtl number is 0.71 for the reference state. If NOB effects are included, the flow pattern P_{11} with only one dominant roll often becomes unstable by the growth of the cold corner roll, which sometimes results in cession-led flow reversals. By exploiting the vorticity transport equation, it is found that the asymmetries of buoyancy and viscous forces are responsible for the growth of the cold corner roll because both such asymmetries cause an imbalance between the corner rolls and the large-scale circulation (LSC). The buoyancy force near the cold wall increases and decreases near the hot wall originating from the temperature-dependent isobaric thermal expansion coefficient $\alpha = 1/T$ if NOB effects are included. Moreover, the decreased dissipation due to lower viscosity is favourable for the growth of the cold corner roll, while the increased viscosity further suppresses the growth of the hot corner roll. Finally, it is found that the boundary layer near the cold wall plays an important role in the mass transport from LSC to corner rolls subject to mass conservation.

Key words: Bénard convection, convection, convection in cavities

1. Introduction

A fascinating dynamic feature of the large-scale circulation in Rayleigh–Bénard convection (RBC) is the cessation and reversal phenomenon, which has been exhibited by many experiments and numerical simulations (see Ahlers, Grossmann & Lohse 2009; Xia 2013, and references therein). It is therefore of great importance to explore the mechanism of the flow reversal phenomenon. For instance, it could provide us with insights into the occasional magnetic polarity reversal associated with convection in the Earth's mantle (Glatzmaier & Roberts 1995; Glatzmaier *et al.* 1999).

There are two categories of flow reversal classified by distinct physical mechanisms. One is rotation-led reversal, which occurs only in a cylinder sample caused by incessant azimuthal meandering of the circulating plane (see Brown & Ahlers 2006,

† Email addresses for correspondence: wanzh@ustc.edu.cn; dsun@ustc.edu.cn

for example). The other is cessation-led reversal, in which large-scale circulation (LSC) sometimes stops and then randomly restarts in a different direction (see Sugiyama *et al.* 2010, for example). The cessation-led reversal can occur both in a cylindrical cell and in a box. In order to explain and predict the observed reversal phenomenon, several theoretical models have been prompted including either stochastic differential equations (Sreenivasan, Bershadskii & Niemela 2002; Benzi 2005; Brown & Ahlers 2007a) or deterministic ones (Fontenele Araujo, Grossmann & Lohse 2005; Resagk *et al.* 2006; Gissinger 2012). The physical model proposed by Sreenivasan *et al.* (2002) showed that the imbalance between buoyancy effects and friction might possibly be responsible for the reversals of LSC. Deriving it directly from the equations of motion, Brown & Ahlers (2007a) proposed a model consisting of two coupled stochastic ordinary differential equations that were able to reproduce some of the important features of the LSC in three-dimensional (3D) RBC, such as cessations and azimuthal meandering. Fontenele Araujo *et al.* (2005) assumed, in their model, that a long-lived plume carried by LSC tends to act against the prevailing flow in the far side. Thus their model is suited to flows with large Prandtl numbers. By incorporating the effects of corner rolls, Ni, Huang & Xia (2015) proposed a stochastic model that bridges the discrepancy found in quasi-two-dimensional (2D) and 3D systems. The experimental study in a 3D box by Huang *et al.* (2015) reported a decoupling of the flow strength and stability of LSC or wind, i.e. reversal behaviour. They claimed that flow reversal is a process of symmetry restoration and found that the more symmetric the system is, the more frequently the flow reversals occur. Later, Huang & Xia (2016) further showed that the reversal frequency increased dramatically in smaller Γ cells and confirmed the conclusion proposed by Ni *et al.* (2015).

Free from complicated and puzzling 3D structures, 2D rectangular samples have been exploited in studying cessation-led reversals (Sugiyama *et al.* 2010; Chandra & Verma 2013; Podvin & Sergent 2015; Verma, Ambhire & Pandey 2015). It is concluded by Sugiyama *et al.* (2010) that two diagonally arranged corner-rolls and moderate Prandtl numbers are necessary in cessation-led reversals. Chandra & Verma (2011, 2013) used the Fourier decomposition method to study the reversals. They proved that flow reversals occur only at a narrow band of Rayleigh numbers with Prandtl numbers equal to 1, where both the Fourier modes (1, 1) and (2, 2) are comparatively strong with nearly equal energy. Podvin & Sergent (2015) applied proper orthogonal decomposition to the velocity and temperature fields of RBC in a 2D square cell. A three-mode model was proposed based on the interaction of the LSC, the quadrupolar flow and horizontal rolls.

Recently, the influence of non-Oberbeck–Boussinesq (NOB) effects on flow dynamics and heat transfer has been studied extensively in turbulent thermal convection (Ahlers *et al.* 2006, 2007, 2008; Brown & Ahlers 2007b; Sugiyama *et al.* 2007, 2009; Sameen, Verzicco & Sreenivasan 2008; Horn, Shishkina & Wagner 2013; Horn & Shishkina 2014). To the best of our knowledge, flow reversals in RBC with NOB effects have not been investigated yet. Therefore, the major objective of this study is to show the scenarios of the flow reversals due to NOB effects, which are quite different in large-scale dynamics from those found under the Oberbeck–Boussinesq (OB) approximation. Moreover, in the NOB case, detailed physical mechanisms of flow reversals are studied from the perspective of vortex dynamics. The remainder of the paper is organized as follows. Section 2 introduces the governing equations and numerical methods. In § 3, the main results are presented and discussed. Finally, a short summary is given in § 4.

2. Governing equations and numerical methods

2.1. Governing equations

Consider thermal convection in a square box with height \hat{H} as the reference length (hatted quantities are dimensional). The bottom and upper walls have high and low constant temperatures \hat{T}_h and \hat{T}_c respectively, the average of which serves as the reference temperature $\hat{T}_0 = (\hat{T}_c + \hat{T}_h)/2$. The side walls are insulated. All four walls are assumed to be no-slip. OB approximation is not applicable for large temperature differences because of the variable physical properties and nonlinear relation between temperature and density in buoyancy force. Thus low-Mach-number equations (Paolucci 1982) are adopted in this paper. Free-fall velocity $\hat{U} = (2\epsilon\hat{g}\hat{H})^{1/2}$ is chosen for the reference velocity with ϵ defined later. Other reference quantities include $\hat{\rho}_0$, $\hat{\rho}_0$, \hat{c}_{p0} , $\hat{\mu}_0$, \hat{k}_0 and \hat{g} . These dimensional quantities are not always independent, e.g. $\hat{p}_0 = \hat{\rho}_0\hat{R}\hat{T}_0$ with \hat{R} the gas constant $8.314 \text{ J K}^{-1} \text{ mol}^{-1}$ and $\hat{\mu}_0$, \hat{k}_0 are functions of \hat{T}_0 at reference state with 300 K, unless otherwise stated. Moreover the dynamic pressure is non-dimensionalized by $\hat{\rho}_0\hat{U}^2$. The non-dimensional low-Mach-number Navier–Stokes (NS) equations in which the acoustic wave is filtered are cast in the form of a Cartesian tensor

$$\frac{\partial \rho}{\partial t} + (\rho u_j)_j = 0, \quad p = \rho T, \quad (2.1)$$

$$\frac{\partial \rho u_i}{\partial t} + (\rho u_i u_j)_j + \pi_{,i} = \left(\frac{Pr}{Ra}\right)^{0.5} \tau_{ij,j} + \frac{1}{2\epsilon}(\rho - 1)n_i, \quad (2.2)$$

$$\rho c_p \left(\frac{\partial T}{\partial t} + u_j T_{,j}\right) = \left(\frac{1}{RaPr}\right)^{0.5} (kT_{,j})_j + \Gamma \frac{dp}{dt}. \quad (2.3)$$

The comma notation for spatial derivatives is adopted, for example, $\pi_{,i} := \partial_i \pi$, which is the gradient of hydrodynamic pressure. ρ is the fluid density, and $u_i = (v, w)$ and $x_i = (y, z)$ are the velocity components and coordinates in the horizontal and vertical directions, respectively. $\tau_{ij} = \mu(u_{i,j} + u_{j,i}) + \lambda \delta_{ij} u_{k,k}$ is the viscosity stress tensor with μ the dynamic viscosity, $\lambda = -2\mu/3$ and δ_{ij} the Kronecker delta function. $n_i = (0, -1)$ is the unit vector in the direction of gravity. $c_p = 1$ is the isobaric specific heat, $\gamma = 1.4$ is the ratio of specific heats, and $\Gamma = (\gamma - 1)/\gamma$ is a measure of the resilience of the fluid. T is temperature, k is thermal conductivity and p is thermodynamic pressure uniform in space and a function of only time. The independent dimensionless parameters characterizing the flow are temperature differential $\epsilon = \Delta\hat{T}/2\hat{T}_0$ with $\Delta\hat{T}$ the dimensional temperature difference between the top and bottom walls, Rayleigh number $Ra = \Delta\hat{T}\hat{c}_{p0}\hat{\rho}_0^2\hat{g}\hat{H}^3/\hat{T}_0\hat{\mu}_0\hat{k}_0$ with \hat{g} the gravity acceleration, and the reference Prandtl number $Pr = \hat{c}_{p0}\hat{\mu}_0/\hat{k}_0 = 0.71$. Temperature differential ϵ is used to quantify the NOB effects. The larger ϵ is, the stronger the NOB effects are. Dimensionless dynamic viscosity μ and conductivity k are computed by Sutherland laws

$$\left. \begin{aligned} \mu &= T^{1.5} \frac{1 + S_\mu}{T + S_\mu}, \\ k &= T^{1.5} \frac{1 + S_k}{T + S_k}, \end{aligned} \right\} \quad (2.4)$$

where $S_k = 0.648$ and $S_\mu = 0.368$ for the reference temperature $T_0 = 300 \text{ K}$. Since $S_k \neq S_\mu$, the Prandtl number is not globally constant. Temperature differential ϵ is

bound to $0.005 \leq \epsilon \leq 0.6$. To achieve OB approximation, we set $\epsilon = 0.005$, $\mu = k = p = 1$, $u_{j,j} = 0$ and $\rho = 1$ except in buoyancy term $\rho = 1 - \Delta T$.

For a closed system with no-slip and no-penetrative boundary conditions, the time derivative of thermodynamic pressure and divergence of velocity are displayed as follows

$$\frac{dp}{dt} = \frac{1}{(1 - \Gamma)V} \left(\frac{1}{RaPr} \right)^{0.5} \oint_S kT_{,j}n_j dS, \tag{2.5}$$

$$u_{j,j} = \frac{1}{p} \left[(\Gamma - 1) \frac{dp}{dt} + \left(\frac{1}{RaPr} \right)^{0.5} (kT_{,j})_{,j} \right]. \tag{2.6}$$

S is the surface surrounding the flow domain with volume V . The total mass M in a closed system is conservative and time-independent. So integrating the equation of state over the whole domain, we obtain the thermodynamic pressure

$$p = M \left(\int_V \frac{dV}{T} \right)^{-1}, \tag{2.7}$$

which is only a function of temperature. Clearly we see that equations (2.1) to (2.3) coupled with (2.5), (2.6) and (2.7) form an integro-differential system, so the aforementioned model equations are global rather than local.

2.2. Numerical method and validation

The low-Mach-number NS equations (2.1)–(2.3) along with proper boundary conditions are solved by the finite difference method. A non-uniform grid with clustered points near walls is adopted to improve the grid resolution. Scalar and vector variables are staggered in space in order to avoid pressure-velocity decoupling. All spatial derivative terms are approximated by a second-order central difference scheme which intrinsically conserves energy. It has been further illustrated by Moin & Verzicco (2016) that staggered second-order finite difference schemes can produce comparatively accurate simulations at lower computational cost. A fractional-step approach is used to solve momentum equations (2.2). Pressure is also staggered in time with other physical variables to further couple pressure-velocity fields. A multi-grid strategy is exploited to accelerate the iteration process in the Poisson equation.

To validate the code called lMn2d, typical cases in thermal convection are computed and compared with existing results. As illustrated in table 1, under OB approximation, the errors between present results and those of de Vahl Davis & Jones (1983) are less than 0.1%. In the NOB case with $\epsilon = 0.6$, our code also gives a relatively small error which is less than 0.1% compared with those of Le Quéré *et al.* (2005). Note that the reference temperature $\hat{T}_0 = 600$ K is just used here and we set $S_\mu = S_k = 0.1842$ in the Sutherland law to keep the Prandtl number constant. Another 2D thermal convection is also preformed in a tall side-heated box with an aspect ratio of length to height $L/H = 1/8$. The oscillating frequency is 3.42 which agrees well with the results in Bathe, Brezzi & Pironneau (2001). For 2D RBC in a square cavity with adiabatic sidewalls, the critical Rayleigh number given by our code is $Ra_c = 2584.12$, which is excellently in agreement with 2585.27 by Sugiyama *et al.* (2009).

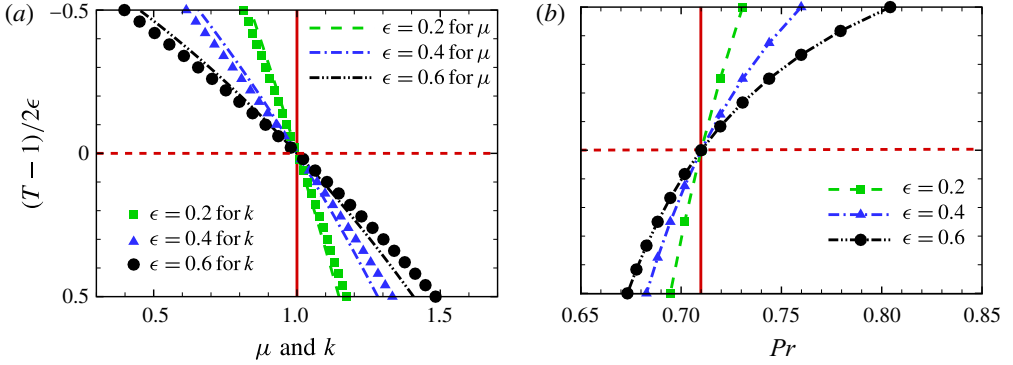


FIGURE 1. (Colour online) (a) μ and k as functions of rescaled T . (b) Pr as a function of rescaled T . Temperature differentials are $\epsilon = 0.2, 0.4$ and 0.6 . Red solid vertical lines show the case under OB approximation for comparison. μ , k and subsequently Pr are all subject to Sutherland laws with reference temperature 300 K.

Ra	10^3	10^4	10^5	10^6	10^6 ($\epsilon = 0.6$)
Nu	1.072	2.056	4.341	8.654	8.694
Ref.	1.071*	2.054*	4.337*	8.640*	8.687 ^b

TABLE 1. Comparison of the averaged Nusselt numbers Nu of the present computations and those of de Vahl Davis & Jones (1983)*, Le Quéré *et al.* (2005)^b.

3. Results and discussion

3.1. Cessation-led reversals by the single corner roll

The Rayleigh number covers a range of $10^5 \leq Ra \leq 5 \times 10^7$. Three meshes have been adopted, the grid points of which are between 128^2 and 384^2 . Since the NOB effects are included, the boundary layer (BL) near the cold wall is much thinner and more grid points should be clustered there. To meet the Courant–Friedrichs–Lewy condition, the time step is of an order of magnitude $O(\Delta x)$, i.e. approximately 10^{-3} dimensionless time unit. The mesh size Δx stringently satisfies the Kolmogorov and Batchelor length scales, both in BLs and bulk regime (Shishkina *et al.* 2010).

3.1.1. Variable physical properties beyond OB approximation

Figure 1 shows that dynamic viscosity μ , conductivity k and also Prandtl number Pr vary with temperature. μ and k are computed with (2.4). As shown in figure 1(a), μ and k vary greatly with T in the NOB case. For example, μ is reduced by more than 50% near the cold wall and increased by approximately 40% near the hot wall when $\epsilon = 0.6$. It is also observed that k varies with T a bit faster than μ . In figure 1(b), Pr also varies with temperature because of the asynchronous changes of μ and k . The red solid vertical line helps to reveal that for the reference state and OB case $Pr = 0.71$. Compared with the OB approximation, the Prandtl number increases near the cold top wall and decreases near the hot bottom wall. Even with $\epsilon = 0.6$, the Prandtl number is approximately 0.8 which is still less than unity, and thus the viscous BL is always nested in the thermal one. Since the change of thermal pressure is relatively small (Le Quéré *et al.* 2005) and perfect gas is used as the working fluid, $\rho = p/T$ becomes

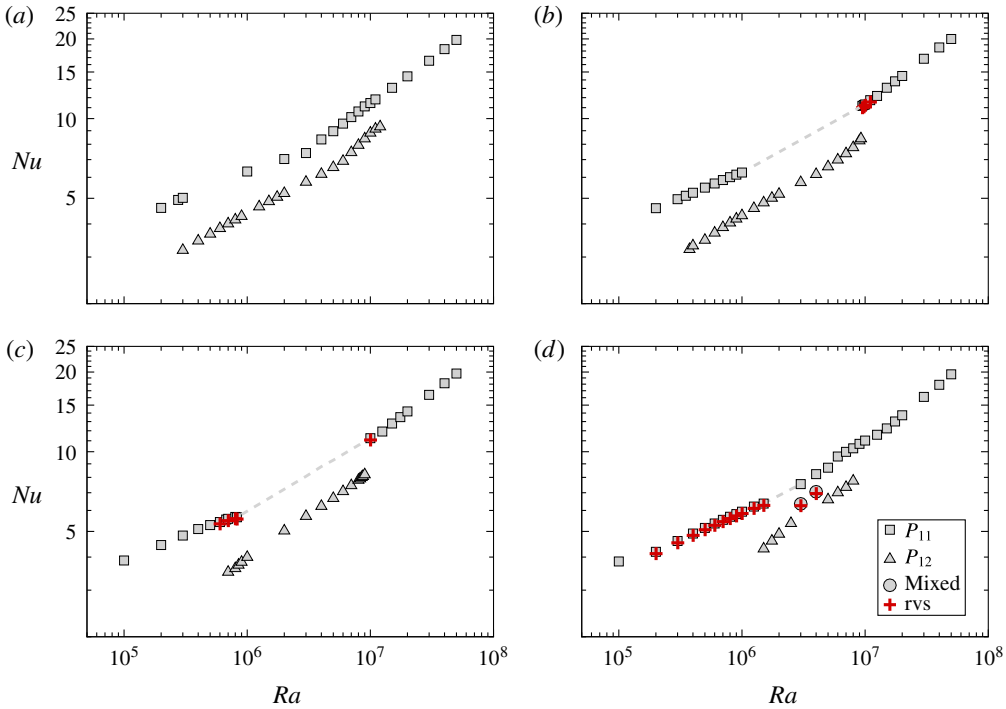


FIGURE 2. (Colour online) Log–log plots of Nu as a function of Ra for various temperature differentials. (a) OB approximation, (b) $\epsilon = 0.2$, (c) $\epsilon = 0.4$, (d) $\epsilon = 0.6$. Grey square symbols are flow pattern P_{11} . Grey triangular symbols are flow pattern P_{12} . Grey circle symbols are specially mixed patterns with both P_{11} with definite period and P_{12} with random period in the process of flow reversals. Red symbols ‘+’ represent where there exist flow reversals and the dashed lines denote that the growth of corner rolls is observed only once and P_{12} is achieved in the end.

larger near the cold wall and smaller near the hot wall. Thus near the cold wall, kinematic viscosity $\nu = \mu/\rho$ becomes smaller and similarly for the thermal diffusivity $\kappa = k/\rho c_p = k/\rho$. Near the hot wall, ν and κ are increased. As regards the thermal isobaric expansion coefficient, clearly $\alpha = 1/T$ becomes larger in magnitude near the cold wall.

3.1.2. New flow reversals

Figure 2 shows plots of Nu as a function of Ra for various temperature differentials and the phenomenon of the co-existence of multiple solutions is identified. In general, two flow patterns P_{11} and P_{12} are identified where P_{11} has one dominant cavity-sizeable roll with two diagonally arranged secondary rolls and P_{12} has two vertically stacked dominant rolls. Under the OB approximation, pattern P_{11} is unchanged in the full Rayleigh number range. When the temperature differential increases, with $\epsilon \geq 0.2$, we observed the corner roll growth at Rayleigh numbers denoted by dashed lines and symbols ‘+’, and the symbols ‘+’ in particular show cases of flow reversals. Phenomenally, flow reversal is caused by corner roll growth. However, corner roll growth does not always result in flow reversal. Dashed lines mean that the corner roll in pattern P_{11} grows in size but ends up with pattern P_{12} . It is conjectured that

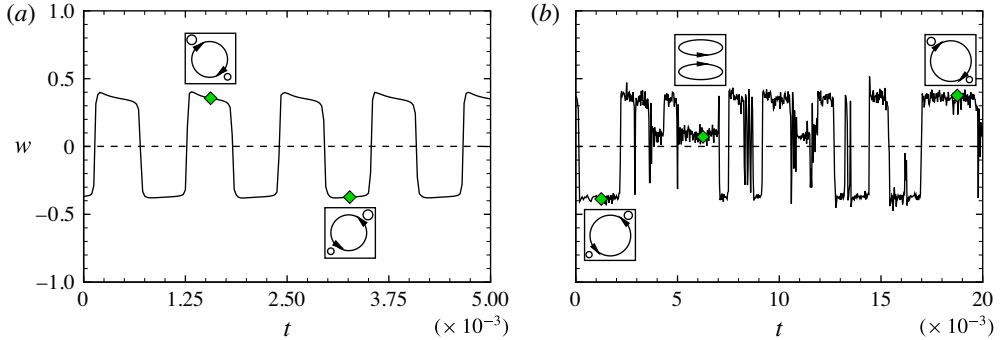


FIGURE 3. (Colour online) Time evolution of vertical velocity component at $(y, z) = (0.1, 0.5)$. (a) $Ra = 7 \times 10^5$, $\epsilon = 0.4$; (b) $Ra = 10^7$, $\epsilon = 0.4$. Green solid diamonds correspond to the closeups near them. In (a), times for the two closeups are 1560 and 3270. In (b), times for the three closeups are 1250, 6250 and 18750. Corresponding flow animations are shown in supplementary movies 1 and 2, available at <http://dx.doi.org/10.1017/jfm.2016.338>.

sometimes, in the phase space the trajectory of pairs of P_{11} passes by the stable pattern P_{12} and is attracted by the stationary point or limiting cycle of P_{12} . In figure 2(d), it is noteworthy that with strong NOB effects two counter-rotating flow patterns P_{11} could switch back and forth with an unstable intermediate pattern P_{12} in $3 \times 10^6 \leq Ra \leq 4 \times 10^6$. In short, as $\epsilon \geq 0.2$, we could observe the growth of the cold corner roll at a large range of Rayleigh numbers, for some of which cession-led flow reversals are clearly found. To some extent, the newly found flow reversals may be related to the tendency for symmetry restoration of an asymmetric system.

Currently, the vertical velocity component w at $y = 0.1$ and $z = 0.5$ is selected as an indicator of flow reversal, since the flow field is well organized by LSC, corner rolls and BLs rather than plumes (Breuer & Hansen 2009; Chandra & Verma 2011). Figure 3(a,b) shows the time evolution of w at $Ra = 7 \times 10^5$ and 10^7 , in which flow reversals can be clearly found. At $Ra = 7 \times 10^5$, the flow is laminar and the period of reversal is definite. At $Ra = 10^7$, the flow is chaotic or turbulent with random periods of reversal. As shown by the inset closeups, at $Ra = 7 \times 10^5$, the flow reversals only include pattern P_{11} which circulates clockwise, counter-clockwise and back (Sugiyama *et al.* 2010; Chandra & Verma 2013). At $Ra = 10^7$, flow pattern P_{12} sometimes appears, which has been recently reported by Podvin & Sergent (2015). In other words, the process of flow reversals in this case contains two flow patterns P_{11} and P_{12} .

3.2. The mechanism of growth of the cold corner roll

3.2.1. Kinematics of reversals

In the work of Sugiyama *et al.* (2010), flow reversals occur due to the growth in size of corner rolls. The flow satisfies top-down symmetry under OB approximation, two diagonally arranged corner rolls grow simultaneously and merge as a new LSC, and finally the preceding LSC is then divided into two new corner rolls (see also Chandra & Verma 2013). When NOB effects are included, the top-down symmetry breaks, which greatly influences the behaviour of large-scale dynamics and consequently flow reversal. Figure 4 shows a half-period of flow reversal for $Ra = 10^7$

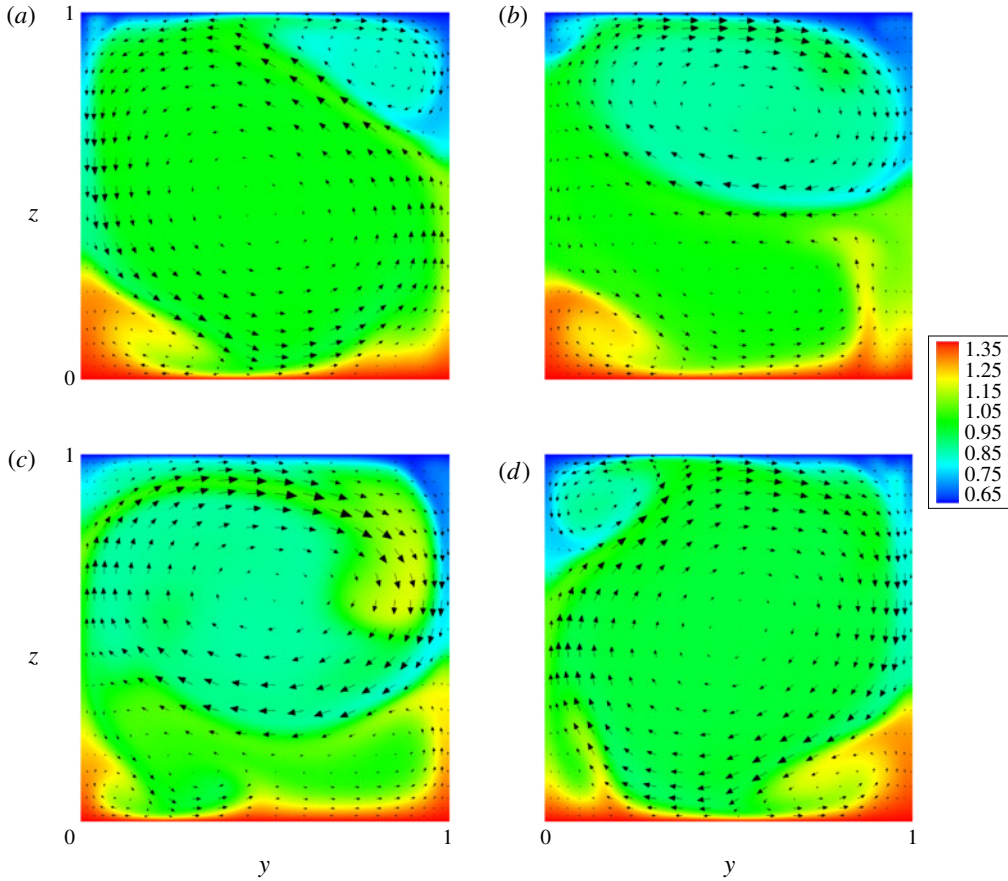


FIGURE 4. (Colour online) Snapshots of four characteristic temperature fields during a half-period of a flow reversal. Red indicates hot fluid and blue cold fluid. Black arrows represent velocity vectors. $Ra = 10^7$, $\epsilon = 0.4$ and the time is near $t = 17\,000$ in figure 3(b).

and $\epsilon = 0.4$. It is found that only the top-right corner roll in figure 4(a), which is larger in size and more energetic than the bottom-left one, grows alone and eventually replaces the LSC. The preceding LSC is divided into two parts. One merges with the existing left hot corner roll and both of them die away finally. The other shrinks to a new hot corner roll near the right wall. Compared with the OB case, two major differences in the reversal process have been identified in the NOB case. On the one hand, the hot corner roll with comparatively small size is weak and no visible expansion is observed. This is caused by both buoyancy reduction and larger viscous dissipation near the bottom wall due to the higher temperature. On the other hand, only the single cold corner roll grows and when it reaches the opposite wall, the buildup of a new cold corner roll can be seen in figure 4(b), which is caused by adverse pressure gradient. As seen in figure 4(c), a portion of descending hot plume is observed near the right wall. Huang & Zhou (2013) found that there exists strong counter-gradient local heat flux with a magnitude much larger than the global Nusselt number Nu . Two mechanisms were proposed to be responsible for the local reverse heat flux. One is due to bulk dynamics and the other comes from the competition between LSC and corner rolls. It is the first mechanism that is recognized presently.

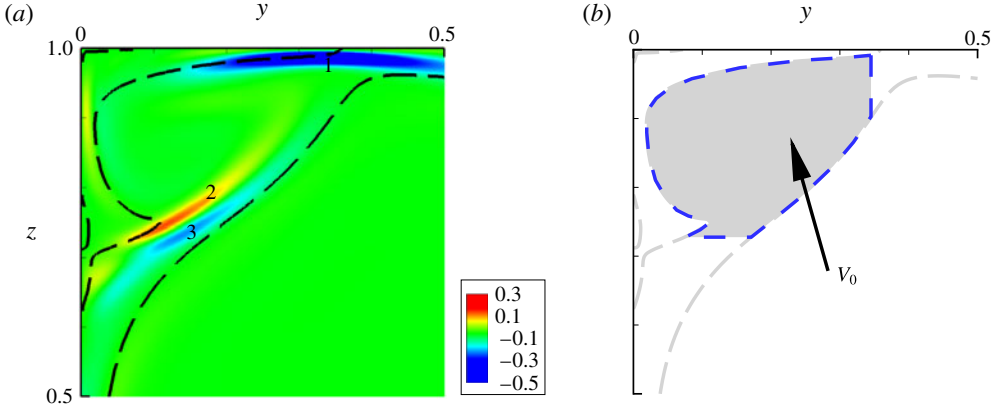


FIGURE 5. (Colour online) (a) Distribution of dilation defined by equation (2.6); only the field of the top-left quarter of the box is shown. $Ra = 10^7$, $\epsilon = 0.4$. (b) Sketch of the control volume related to (a). The time is the same as figure 4(d). Dashed lines are contours of vorticity density of zero value and roughly serve as dividing lines between LSC and corner rolls.

This descending hot plume forced by the velocity field originated from the newly formed bulk produces counter-gradient local heat flux which results in even negative average Nu (Chandra & Verma 2013; Yanagisawa, Hamano & Sakuraba 2015; Huang & Xia 2016).

3.2.2. Physical mechanism from dynamics of vorticity transport

As aforementioned, the growth of the single cold corner roll induces flow reversals when NOB effects are included, but the physical mechanisms corresponding to the corner roll growth have not yet been analysed. In this subsection, we attempt to understand the detailed mechanisms of growth of the cold corner roll from the perspective of vortex dynamics. First, based on the low-Mach-number momentum equations (2.2) and Reynolds transport theorem, we derive the vorticity transport equation in the NOB case. It is believed that vorticity in corner rolls and LSC is in dynamic balance under OB approximation. And thus possibly the balance is broken by vorticity generation in corner rolls when flow reversals occur with NOB effects. Our aim is to pinpoint which terms in this equation are dominant for the vorticity generation in the corner roll. The vorticity transport equation can be expressed as

$$\begin{aligned} \frac{\partial}{\partial t} \int_{V_0} dV \Omega_i = & \underbrace{- \oint_{S_0} n_j dS \Omega_i u_j}_{\text{I}} - \underbrace{\int_{V_0} dV \Omega_i \partial_j u_j}_{\text{II}} - \underbrace{\int_{V_0} dV \frac{1}{T} \mathbf{e}_{ijk} \partial_j T \partial_k \pi}_{\text{III}} \\ & + \underbrace{\left(\frac{Pr}{Ra} \right)^{0.5} \int_{V_0} dV \frac{1}{T} \mathbf{e}_{ijk} \partial_j (T \partial_l \tau_{lk})}_{\text{IV}} - \underbrace{\frac{1}{2\epsilon} \int_{V_0} dV \frac{1}{T} \mathbf{e}_{ijk} \partial_j T n_k}_{\text{V}}, \quad (3.1) \end{aligned}$$

where S_0 and V_0 are the control surface and volume in figure 5(b). The control volume in (3.1) is roughly surrounded by the zero-value vorticity lines near the top-left corner and two other straight lines $y \approx 0.35$ and $z \approx 0.75$. Since 2D RBC is considered, the

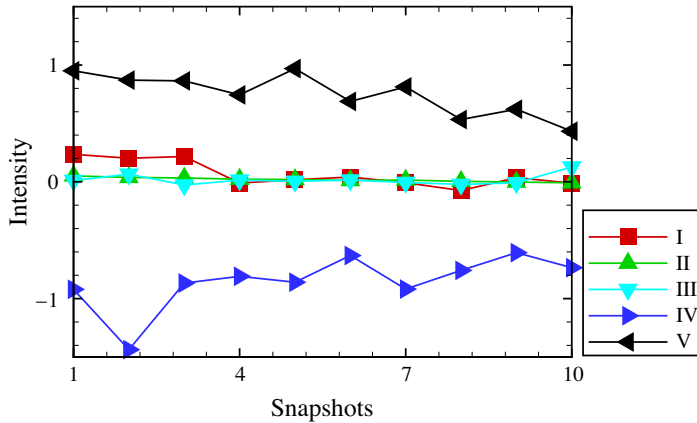


FIGURE 6. (Colour online) Intensities of contributions to the time rate of change of vorticity in the control volume in ten snapshots. The intensities are normalized by the grey area in figure 5(b) for integration. $Ra = 10^7$, $\epsilon = 0.4$.

term ‘control volume’ is actually a fixed area and S_0 the line surrounding it. With no stretching and tilting of the vortex filament, $\Omega_i = \rho\omega_i$ is the vorticity density with $i = 1$ in 2D simulation. ϵ_{ijk} is the permutation tensor. The left integral term is the time rate of change of total vorticity surrounded by S_0 . On the right-hand side of the equality, term I means vorticity transport by convection; term II represents the change of vorticity by dilation or compressibility, vanishing under the OB limit; term III is the interaction of gradient of temperature and hydrodynamic pressure, i.e. baroclinity; term IV is the vorticity diffusion by viscous force; and the last term V indicates the vorticity generation by buoyancy force.

Figure 5(a) shows distributions of dilation for $Ra = 10^7$ with $\epsilon = 0.4$. LSC and corner rolls could be divided by black-dashed auxiliary vorticity contour lines with zero value. Qualitatively, term I becomes stronger when the Rayleigh number increases and subsequently more plumes detach from the unstable corner roll. For term II, the maximum and minimum regions of dilation in figure 5(a), denoted ‘1’, ‘2’ and ‘3’, are all approximately within the corner roll. The zero contour line of vorticity density goes through ‘1’. The maximum ‘2’ and minimum ‘3’ are near each other, and thus their contributions would approximately offset each other. Since low-Mach-number flow with large temperature difference is barotropic, term III, baroclinity, may possibly change with temperature gradient. The contribution should be specified quantitatively. Term IV, associated with viscosity force, is always negative, corresponding to the vorticity diffusion and dissipation. When the Rayleigh number increases, the viscous effect decreases and concentrates near the wall and the thin region between the corner rolls and LSC. The last term, V, shows the interaction between gravity and temperature gradient. When NOB effects become stronger, it can be affected by $T_{,i}/2\epsilon$ and the reciprocal of temperature $1/T$. The coefficient $1/T$ of terms III and V introduces some extent of asymmetry between the diagonally arranged top and bottom corner rolls. The asymmetry in term IV is μ in τ_{ij} rather than $1/T$.

To quantify the contributions of the five terms in (3.1) to the time rate of change of vorticity, we compute their normalized intensities in ten snapshots at $Ra = 10^7$ with $\epsilon = 0.4$ in figure 6. Ten snapshots with an equal time interval are carefully chosen to ensure that they are all at the initial phase of a flow reversal. Compared to the

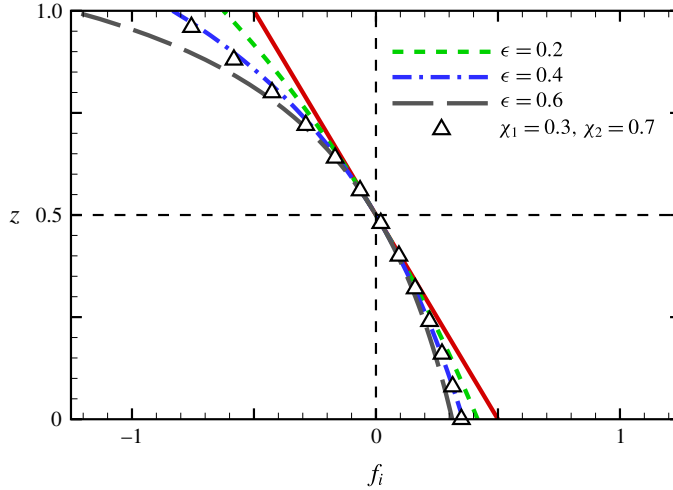


FIGURE 7. (Colour online) Buoyancy force $f_i = (\rho - 1)n_i/2\epsilon$ varying with height z providing linear distribution of temperature $T = 1 + \epsilon(1 - 2z)$. The black hollow up-triangles represent the distribution of equivalent buoyancy force with respect to the reference state with modelled gravity acceleration. The red solid line is to show the case under OB approximation for comparison.

duration of growth of corner rolls, the ten snapshots are taken within a short time. In general, terms IV and V are dominant. From flow fields, term I is found to be related to the oscillations of unstable corner rolls where plume detachment from the corner rolls by convection causes vorticity and energy loss. The plume detachment could also be found in the OB case (Sugiyama *et al.* 2010). Plume detachment occurs frequently, which could interrupt the growth of corner rolls whether or not NOB effects are included. In NOB cases, term II is small and negligible, which is consistent with the previous qualitative analysis. Term III is of an order of magnitude of 0.01 and thus can be neglected as well. This is because the temperature gradient within the cold corner rolls may still be small and so is the gradient of velocity, although ϵ is increased up to 0.4.

As stated previously, the interesting difference is that only the cold corner roll grows, while the hot corner roll is found to be nearly quiescent. As we can see in figure 6, terms IV and V are two decisive factors. It is obvious that term V is always positive and thus of vital importance in vorticity generation. The asymmetries caused by $1/T$ (isobaric thermal expansion coefficient $\alpha = 1/T$) in this term other than $1/T_0 = 1$ under OB approximation may play key roles in the growth of the cold corner roll. Term V originates from the buoyancy force $f_i = \delta\rho n_i/2\epsilon$ in (2.2). Under the OB approximation, $f_i = -\delta T n_i/2\epsilon$ is proportional to δT while this relation does not hold in the NOB case $f_i = (1/T - 1)n_i/2\epsilon \approx (-\delta T + \delta^2 T)n_i/2\epsilon$ with $\delta T = T - 1$. In figure 7, due to NOB-effects-led asymmetry, the buoyancy force has increased by up to 150% on the cold wall and reduced by approximately 40% near the hot wall. Equivalently, we modified the gravity acceleration to model a similar buoyancy force based on the OB approximation. In figure 7, the up-triangular symbols display a buoyancy force to model that of $\epsilon = 0.4$. The expression of acceleration is $f_i = -\delta T(n_i + dg_i)/2\epsilon$ with $dg_i = -2.0\chi z + \chi$ in which $\chi = \chi_1 = 0.3$ when $z \leq 0.5$ and $\chi = \chi_2 = 0.7$ when $z > 0.5$. By adding this equivalent buoyancy force to the OB case, not surprisingly, we

reproduced flow reversals (see supplementary movie 3). In this case, the hot corner roll still grows at a smaller rate than its cold counterpart, although the buoyancy force is reduced near the hot wall. The modified buoyancy force by NOB effects increases the probability of the balance breaking (Sreenivasan *et al.* 2002; Liu *et al.* 2008) between the corner roll and LSC, and thus leads to flow reversal. In addition, the variation in viscous dissipation in term IV by NOB effects, as seen in figure 1, is also very important for the growth of the cold corner roll. Near the hot wall, viscous dissipation is largely enhanced, which helps to suppress the growth of the hot corner roll. Conversely, the viscous dissipation near the cold wall is considerably attenuated, which promotes the growth of the cold corner roll. Moreover, it is noteworthy that thermal conductivity k is also temperature-dependent. Although thermal conductivity k does not appear explicitly in vorticity transport equation (3.1), as stated by Sugiyama *et al.* (2010), small k near the cold wall has small thermal dissipation similar to μ . In figure 1(b), the Prandtl number does not change much and is always smaller than one. Therefore the effect of change of the Prandtl number could probably be ignored.

3.2.3. Mass transport and the role of BLs

In the previous section, we conclude that the asymmetry of isobaric thermal expansion coefficient $\alpha = 1/T$ is the point that results in the growth of the cold corner roll. A very important issue, from the point of view of conservation, is that the process of mass transport between corner rolls and other regimes is still unknown. Figure 8 shows the distribution of density near the top-left corner and the trajectories of two ‘tracer particles’. The trajectories are computed by the predictor–corrector method with accuracy of second order, which is consistent with that of the present code. The corner roll and LSC interact with the top wall and two parts of the BLs form with the joint point marked ‘O’. When the corner roll grows, point ‘O’ moves rightward. Figure 8(a) shows that the density in the cold corner roll changes from 1.6 to approximately 1. The initial positions of the tracer particles are located on either side of the joint point ‘O’. In figure 8(b), tracer particle ‘A’ is initially located in the left part of the BL and we find that it always circles in the corner roll and is superimposed by a small velocity pointing to LSC, corresponding to the expansion of the corner roll. The tracer particle ‘B’ is located initially in the right part of the BL related to LSC. It is found that the tracer particle ‘B’ moves rightward initially (black arrow in figure 8(c)) and circles the bulk. After six rounds, when the time is approximately 390 in figure 8(c), tracer particle ‘B’ turns left into the corner roll at the seventh round. At this moment, the flow field shows us that the joint point ‘O’ has a horizontal location $y \approx 0.5$ so that particle ‘B’ just after the six rounds has been contained in the left part of the BL. The trajectory of tracer particle ‘B’ clearly shows how the fluid parcel transports from LSC into the cold corner roll. This process could partially explain why the cold corner roll grows from the point of view of mass conservation. Then, it is easy to imagine that when the joint point ‘O’ moves to $y = 1$, all the fluid parcels in the BL would transport into the cold corner roll and the preceding bulk could eventually be replaced. Moreover, the asymmetry by NOB effects manifests itself as a thinner BL near the cold upper plate. We could speculate that the relatively small viscosity there helps to transport mass from the BL to the corner roll.

4. Summary and conclusion

In this work, by employing low-Mach-number NS equations, we focus on studying flow reversals in 2D RBC, considering the NOB effects caused by large temperature difference. In OB cases, no flow reversal is found in the present parameter space.

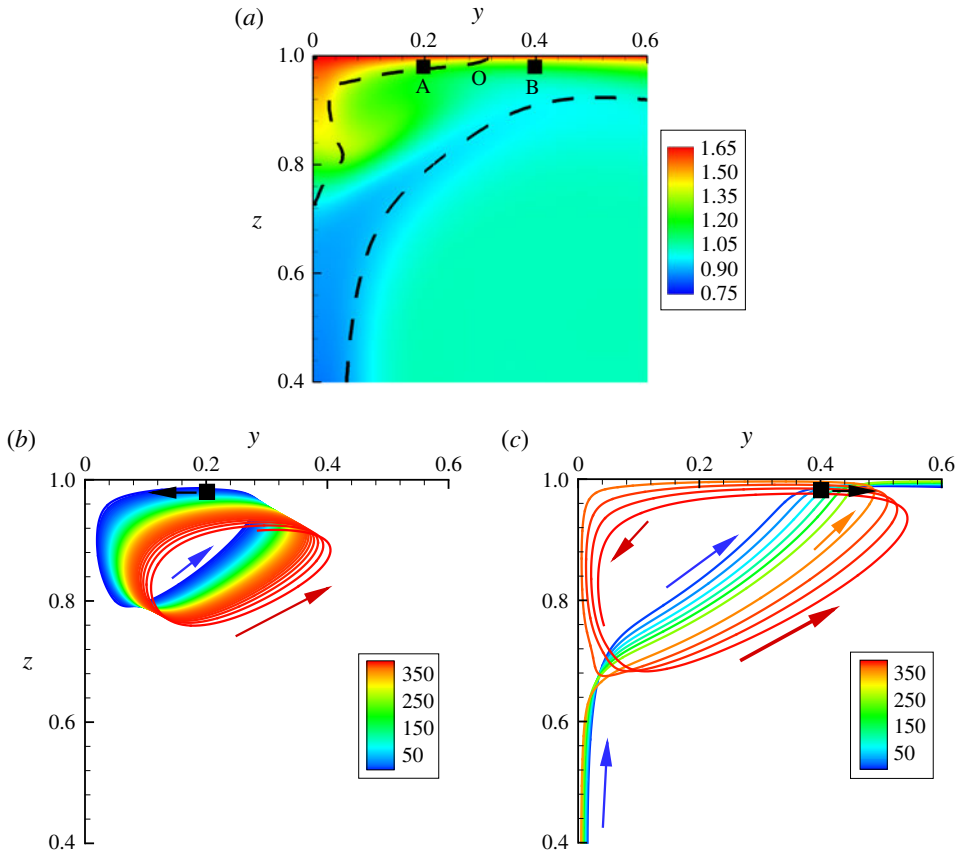


FIGURE 8. (Colour online) (a) Distribution of density near top-left corner. (b) Trajectory of ‘tracer particle’ A for time duration of 400 dimensionless time units. (c) Trajectory of ‘tracer particle’ B for time duration of 400 dimensionless time units. $Ra = 7 \times 10^5$, $\epsilon = 0.4$. Initial coordinates of A and B are $y = 0.1978$, $z = 0.9862$ and $y = 0.3974$, $z = 0.9862$, respectively shown as black squares. The initial directions are also shown in (b) and (c) and the nearby black arrows reveal the moving directions at the beginning.

Interestingly, once the NOB effects are included, flow reversals are observed for certain ranges of Rayleigh number. Moreover, it is found that the flow reversal occurring at low Ra usually has a definitive period, while this period tends to be random with increasing Ra . In general, as the temperature differential ϵ increases, the parameter range of Ra in which the corner roll grows and flow reversals occur is widened. This can be viewed as a symmetry restoration process. Phenomenally, in NOB cases, all flow reversals are led by growth of the single cold corner roll, which is quite different from that in OB cases. From the perspective of vortex dynamics, we find that the asymmetries of buoyancy force by variable isobaric thermal coefficient, temperature-dependent viscosity are the major reason why only the cold corner roll grows and eventually replaces the LSC, resulting in flow reversals. In the NOB case, the buoyancy force is increased and viscous dissipation is greatly reduced near the cold wall, both of which are beneficial for the growth of the cold corner roll and thus increase the probability of flow reversals. Lastly, from examining the trajectories

of tracer particles, we find that the rightward-moving joint point separating the two sections of BLs near the cold wall plays an important role in mass transport from LSC to corner roll.

Acknowledgements

The authors appreciate the reviewers' constructive comments and suggestions that helped to improve the manuscript. We thank Dr B. Wang at Durham University for helpful discussions. This work was supported by the National Natural Science Foundation of China under grant nos. 11572314, 11232011 and 11402262, and the Fundamental Research Funds for the Central Universities.

Supplementary movies

Supplementary movies are available at <http://dx.doi.org/10.1017/jfm.2016.338>.

REFERENCES

- AHLERS, G., ARAUJO, F. F., FUNFSCHILLING, D., GROSSMANN, S. & LOHSE, D. 2007 Non-Oberbeck–Boussinesq effects in gaseous Rayleigh–Bénard convection. *Phys. Rev. Lett.* **98** (5), 054501.
- AHLERS, G., BROWN, E., ARAUJO, F. F., FUNFSCHILLING, D., GROSSMANN, S. & LOHSE, D. 2006 Non-Oberbeck–Boussinesq effects in strongly turbulent Rayleigh–Bénard convection. *J. Fluid Mech.* **569**, 409–445.
- AHLERS, G., CALZAVARINI, E., ARAUJO, F. F., FUNFSCHILLING, D., GROSSMANN, S., LOHSE, D. & SUGIYAMA, K. 2008 Non-Oberbeck–Boussinesq effects in turbulent thermal convection in ethane close to the critical point. *Phys. Rev. E* **77** (4), 046302.
- AHLERS, G., GROSSMANN, S. & LOHSE, D. 2009 Heat transfer and large scale dynamics in turbulent Rayleigh–Bénard convection. *Rev. Mod. Phys.* **81** (2), 503.
- BATHE, K.-J., BREZZI, F. & PIRONNEAU, O. 2001 *Computational Fluid and Solid Mechanics*, vol. 2. Springer.
- BENZI, R. 2005 Flow reversal in a simple dynamical model of turbulence. *Phys. Rev. Lett.* **95** (2), 024502.
- BREUER, M. & HANSEN, U. 2009 Turbulent convection in the zero Reynolds number limit. *Eur. Phys. Lett.* **86** (2), 24004.
- BROWN, E. & AHLERS, G. 2006 Rotations and cessations of the large-scale circulation in turbulent Rayleigh–Bénard convection. *J. Fluid Mech.* **568**, 351–386.
- BROWN, E. & AHLERS, G. 2007a Large-scale circulation model for turbulent Rayleigh–Bénard convection. *Phys. Rev. Lett.* **98** (13), 134501.
- BROWN, E. & AHLERS, G. 2007b Temperature gradients, and search for non-Boussinesq effects, in the interior of turbulent Rayleigh–Bénard convection. *Eur. Phys. Lett.* **80** (1), 14001.
- CHANDRA, M. & VERMA, M. K. 2011 Dynamics and symmetries of flow reversals in turbulent convection. *Phys. Rev. E* **83** (6), 067303.
- CHANDRA, M. & VERMA, M. K. 2013 Flow reversals in turbulent convection via vortex reconnections. *Phys. Rev. Lett.* **110** (11), 114503.
- FONTELENE ARAUJO, F., GROSSMANN, S. & LOHSE, D. 2005 Wind reversals in turbulent Rayleigh–Bénard convection. *Phys. Rev. Lett.* **95** (8), 084502.
- GISSINGER, C. 2012 A new deterministic model for chaotic reversals. *Eur. J. Mech. B* **85** (4), 1–12.
- GLATZMAIER, G. A., COE, R. S., HONGRE, L. & ROBERTS, P. H. 1999 The role of the Earth's mantle in controlling the frequency of geomagnetic reversals. *Nature* **401** (6756), 885–890.
- GLATZMAIER, G. A. & ROBERTS, P. H. 1995 A three-dimensional self-consistent computer simulation of a geomagnetic field reversal. *Nature* **377**, 203–209.

- HORN, S. & SHISHKINA, O. 2014 Rotating non-Oberbeck–Boussinesq Rayleigh–Bénard convection in water. *Phys. Fluids* **26** (5), 055111.
- HORN, S., SHISHKINA, O. & WAGNER, C. 2013 On non-Oberbeck–Boussinesq effects in three-dimensional Rayleigh–Bénard convection in glycerol. *J. Fluid Mech.* **724**, 175–202.
- HUANG, S.-D., WANG, F., XI, H.-D., XIA, K.-Q. & OTHERS 2015 Comparative experimental study of fixed temperature and fixed heat flux boundary conditions in turbulent thermal convection. *Phys. Rev. Lett.* **115** (15), 154502.
- HUANG, S.-D. & XIA, K.-Q. 2016 Effects of geometric confinement in quasi-2-D turbulent Rayleigh–Bénard convection. *J. Fluid Mech.* **794**, 639–654.
- HUANG, Y.-X. & ZHOU, Q. 2013 Counter-gradient heat transport in two-dimensional turbulent Rayleigh–Bénard convection. *J. Fluid Mech.* **737**, R3.
- LE QUÉRÉ, P., WEISMAN, C., PAILLÈRE, H., VIERENDEELS, J., DICK, E., BECKER, R., BRAACK, M. & LOCKE, J. 2005 Modelling of natural convection flows with large temperature differences: a benchmark problem for low Mach number solvers. Part 1: reference solutions. *Math. Modelling Numer. Anal.* **39** (03), 609–616.
- LIU, B., ZHANG, J. & OTHERS 2008 Self-induced cyclic reorganization of free bodies through thermal convection. *Phys. Rev. Lett.* **100** (24), 244501.
- MOIN, P. & VERZICCO, R. 2016 On the suitability of second-order accurate discretizations for turbulent flow simulations. *Eur. J. Mech. B* **55**, 242–245.
- NI, R., HUANG, S.-D. & XIA, K.-Q. 2015 Reversals of the large-scale circulation in quasi-2D Rayleigh–Bénard convection. *J. Fluid Mech.* **778**, R5.
- PAOLUCCI, S. 1982 Filtering of sound from the Navier–Stokes equations. *NASA STI/Recon Tech. Rep. N*, 83, 26036.
- PODVIN, B. & SERGENT, A. 2015 A large-scale investigation of wind reversal in a square Rayleigh–Bénard cell. *J. Fluid Mech.* **766**, 172–201.
- RESAGK, C., DU PUIITS, R., THESS, A., DOLZHANSKY, F. V., GROSSMANN, S., ARAUJO, F. F. & LOHSE, D. 2006 Oscillations of the large scale wind in turbulent thermal convection. *Phys. Fluids* **18** (9), 095105.
- SAMEEN, A., VERZICCO, R. & SREENIVASAN, K. R. 2008 Non-Boussinesq convection at moderate Rayleigh numbers in low temperature gaseous helium. *Phys. Scr.* **2008** (T132), 014053.
- SHISHKINA, O., STEVENS, R. J. A. M., GROSSMANN, S. & LOHSE, D. 2010 Boundary layer structure in turbulent thermal convection and its consequences for the required numerical resolution. *New J. Phys.* **12** (7), 075022.
- SREENIVASAN, K. R., BERSHADSKII, A. & NIEMELA, J. J. 2002 Mean wind and its reversal in thermal convection. *Phys. Rev. E* **65** (5), 056306.
- SUGIYAMA, K., CALZAVARINI, E., GROSSMANN, S. & LOHSE, D. 2007 Non-Oberbeck–Boussinesq effects in two-dimensional Rayleigh–Bénard convection in glycerol. *Eur. Phys. Lett.* **80** (3), 34002.
- SUGIYAMA, K., CALZAVARINI, E., GROSSMANN, S. & LOHSE, D. 2009 Flow organization in two-dimensional non-Oberbeck–Boussinesq Rayleigh–Bénard convection in water. *J. Fluid Mech.* **637**, 105–135.
- SUGIYAMA, K., NI, R., STEVENS, R. J. A. M., CHAN, T. S., ZHOU, S.-Q., XI, H.-D., SUN, C., GROSSMANN, S., XIA, K.-Q. & LOHSE, D. 2010 Flow reversals in thermally driven turbulence. *Phys. Rev. Lett.* **105** (3), 034503.
- DE VAHL DAVIS, G. & JONES, I. P. 1983 Natural convection in a square cavity: a comparison exercise. *Intl J. Numer. Meth. Fluids* **3** (3), 227–248.
- VERMA, M. K., AMBHIRE, S. C. & PANDEY, A. 2015 Flow reversals in turbulent convection with free-slip walls. *Phys. Fluids* **27** (4), 047102.
- XIA, K.-Q. 2013 Current trends and future directions in turbulent thermal convection. *Theor. Appl. Mech. Lett.* **3** (5), 052001.
- YANAGISAWA, T., HAMANO, Y. & SAKURABA, A. 2015 Flow reversals in low-Prandtl-number Rayleigh–Bénard convection controlled by horizontal circulations. *Phys. Rev. E* **92** (2), 023018.